Martensite Decomposition and Ultrafine Grain Formation during Small Punch Creep Testing of Additively Manufactured Ti64

Mathieu Lalé, Benaissa Malek, Bernard Viguier

metals

MDPI

Article

Martensite Decomposition and Ultrafine Grain Formation during Small Punch Creep Testing of Additively Manufactured Ti64

Mathieu Lalé *, Benaissa Malek and Bernard Viguier

CIRIMAT, Toulouse INP, Université Toulouse 3 Paul Sabatier, CNRS, Université de Toulouse, 4 allée Emile Monso-BP44362, CEDEX 4, 31030 Toulouse, France; bernard.viguier@toulouse-inp.fr (B.V.)
* Correspondence: mathieu.lale@toulouse-inp.fr

Abstract: The creep behaviour of as-built additive-manufactured Ti-6Al-4V alloy was studied through small punch creep test (SPCT) experiments at 450 and 500 °C. The couple stress/minimum strain rate deduced from these tests made it possible to draw a Norton plot showing good agreement with tensile test creep results. The microstructure characterisation within the SPCT specimen evidenced the effect of local strain on microstructure evolution. After interrupted creep at 450 °C, in most deformed areas, the as-built martensite structure was fully decomposed to the α + β equilibrium phases, giving rise to a submicron equiaxed grain structure.

Keywords: titanium alloys; small punch creep test (SPCT); creep; martensitic phase transformation; ultrafine microstructure

Citation: Lalé, M.; Malek, B.; Viguier, B. Martensite Decomposition and Ultrafine Grain Formation during Small Punch Creep Testing of Additively Manufactured Ti64. *Metals* **2023**, *13*, 1657. https://doi.org/10.3390/met13101657

Academic Editor: Shili Shu

Received: 31 August 2023
Revised: 22 September 2023
Accepted: 26 September 2023
Published: 27 September 2023

1. Introduction

Due to the combination of very good mechanical properties, low density, and high corrosion resistance and biocompatibility, titanium alloys are commonly used in a wide range of industrial fields, such as aerospace, health, and chemistry [1]. Among titanium alloys, the most widely used is by far the Ti-6Al-4V alloy (Ti64), which has been called the workhorse of the titanium industry [2]. This alloy is usually obtained via conventional cast and wrought processes, and industrial parts are manufactured through material removal machining. The more recent development of additive manufacturing (AM) processes has had a strong impact on the production of Ti64 alloy parts by means of various techniques such as laser–powder bed fusion (L-PBF), through which complex parts are built layer by layer. The very fast cooling rate associated with this process results in a very fine fully martensitic α′ microstructure, in contrast to the classical α + β microstructures obtained through classical thermomechanical processing. Such an AM as-built martensitic microstructure is also recognised to be out of equilibrium, and the martensite may evolve to further decompose and form the more stable α + β microstructure. The progress of decomposition, as well as its kinetics, depends of course on thermal conditions but can also be influenced by the local mechanical state. The L-PBF process also induces a strongly anisotropic structure due to the solidification of large β grains through the successive layers along the building direction. These grains are then transformed into martensite during rapid cooling. The microstructure may depend on the local thickness and fabrication path within the final part [3]. Several authors assessed this purpose in the literature. For example, in a complex industrial part such as a rocket engine impeller, it was shown by Barriobero-Vila et al. [4] that the microstructure and thus the material properties may strongly depend on the local thermal history during part fabrication. The authors showed that in regions in contact with the powder bed (downskin regions), for which heat transfer is less important, the amount of β phase could reach 4–6 vol%. Munk et al. worked on the effect of the built geometry on both microstructure and mechanical properties. Two

geometries were printed. The reference geometry is a constant cross-section cylinder. The second geometry is a cylinder with a small cross-section and whose upper layers have an increased cross-section due to an increased diameter. This last geometry exhibits heat transfer gradient due to varying the cross-section. The evolution of the microstructure was studied along the heat transfer gradient zone. Zones with less heat transfer showed higher β phase fraction. This amount varies from 0% to 20% within only 5 mm [5]. For these reasons, it seemed important to use methods to probe the mechanical properties of the material locally. The small punch testing method may be relevant for this purpose, and its applicability is worth investigating. This method, which was initially developed for the nuclear industry, consists of punching a disc of 10 mm in diameter and 0.5 mm in thickness with a hemispherical tip [6,7]. It is thus very easy to take specimens on different positions and orientations. The method was first developed on an imposed displacement rate mode in order to characterize the yield of the material, mainly on nuclear industry steels [8]. The method then evolved for testing different materials such as Al [9], Mg [10], Ni [11], or Fe-Al [12]-based alloys or composites. It was also used on load control mode to test the creep behaviour of the material; this latter technique is known as small punch creep testing (SPCT). The creep technique was already presented in the good practice guidelines [13] and is further developed in the more recent standard to the small punch methods [14]. The SPCT technique was mainly used for studying the creep properties of power plant steels [8,13,15–19] and has recently been extended to the study of nickel-based superalloys [20]. Regarding the behaviour of the Ti64 alloy, the small punch technique was used to study yielding in both wrought and AM elaborated materials through SPT testing [21–23]. However, the creep behaviour of AM Ti64 was only studied using uniaxial tests either in compression or tensile mode [24–26]. To the author's knowledge, no study of the creep properties of additive manufactured Ti64 alloy using the SPCT technique has yet been published.

The purpose of the present study is to verify the possibilities of investigating L-PBF Ti64 through SPCT and to check if the results are consistent with uniaxial creep testing. Moreover, we would take advantage of the variety of mechanical states, in terms of strain and stress, over the SPCT specimen to investigate the role of creep on phase transformation and martensite decomposition.

2. Materials and Methods

For the present study, we elaborated cylindrical specimens of Ti64 alloy through additive manufacturing using the L-PBF technique. We used a gas atomised Ti-6Al-4V powder in the size range 15–45 µm from Oerlikon^{TM} and a COHERENT CREATOR machine. The powder bed was pre-heated at 80 °C in the chamber that was filled with Ar gas. The manufacturing parameters were as follows: laser power, 93 W; scan speed, 500 mm/s; hatch space, 50 µm; layer thickness, 25 µm; and spot diameter, 40 µm; resulting in an energy density of 148.8 J/mm^3. Cylinders of 10 mm diameter and 40 mm length were manufactured normal to the building plate so that the cylinder axis was along the building direction. For SPCT experiments, 0.7 mm thick slices were cut using an electro-discharge machine in order to avoid mechanical damage to the sample surfaces that might have resulted from machining using conventional cutting tools. The disks were ground down to 500 µm thick, removing 100 µm on each side to get rid of the heat-affected zone from the cutting process. Final polishing was achieved using P4000 SiC abrasive paper for the surface in contact with the punch and complemented by Oxide Polishing Suspension for the opposite surface. The thickness of the specimen was controlled throughout the polishing process using a Mitutoyo palmer micrometer. Special preparation was carried out for EBSD analysis. Interrupted test specimens were cross-sectioned via diamond wire saw close to top of the punching dome. They were then clamped between non-magnetic rings, followed by the embedding process in a phenol formol GEPD/Ca ESCIL resin, and finally ground until the observation surface corresponds to the actual deformation dome. The analysed surface was polished with P2400 abrasive SiC paper. The final polishing step was achieved

thanks to a diluted solution of oxide polishing suspension and hydrogen peroxide H_2O_2 (70 mL + 30 mL) for 35 min.

The microstructure was examined using a scanning electron microscope (SEM) from Centre de Microcaractérisation Raimond Castaing, Toulouse, France. A Jeol 7800F microscope equipped with a field emission gun was used for high-resolution imaging. A Jeol JSM 7100F equipped with a CMOS electron back-scattered diffraction (EBSD) detector (Symmetry S2, Oxford Instruments, Abingdon, UK) and Aztec 5.0 acquisition software was used for grain and misorientation analysis. An accelerating voltage of 20 kV, a probe current of 13 nA, and a working distance of 15 mm were used. The microstructure of the as-built state is presented in Figure 1. It is fully martensitic (α′) and exhibits numerous twins within α′ laths. This out-of-equilibrium microstructure is related to high cooling rates (10^5–10^7 K/s), as commonly observed [27,28].

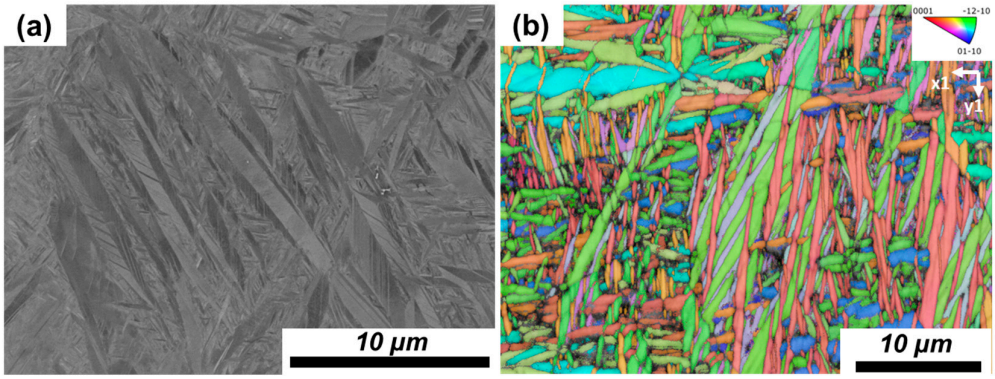

Figure 1. Martensitic microstructure of the tested material within the plane perpendicular to the building direction: (**a**) BSE image and (**b**) IPF-Z.

Mechanical testing through SPCT was performed on a dedicated rig mounted on a Zwick Roell Z010 electrically driven testing machine. Further details on the experimental rig have been presented elsewhere [29]. The disk specimen was placed at the centre of a three-zone light furnace but not directly exposed to the lamp's radiation. Three thermocouples fixed in the chamber allowed to monitor the specimen temperature, heating was performed at 10 K/min, and the specimen was held at the test temperature for 10 min prior the test for temperature homogenisation. SPCT experiments were performed under constant load; the target load was obtained under the displacement motion of the punch at 0.2 mm/min, and then the machine was switched to load control mode. The value of the load (F_{intial}) was calculated from the target nominal initial stress ($\sigma_{initial}$) according to the European Code of Practice's semi-empirical relationship [13]:

$$F_{initial} = \sigma_{initial} * 3.33 * k_{SP} \frac{r^{1.2} h_0}{(0.5 * D)^{0.2}} \quad (1)$$

where D is the receiving hole diameter, h_0 is the initial sample thickness, and r is the punch radius. SPCT has been performed at 450 and 500 °C under initial stresses ranging from 350 MPa to 450 MPa. The testing temperatures were selected, first of all, because they correspond to the maximum operating temperature for parts made of Ti64 alloys. This temperature is also a compromise. Indeed, on the one hand, the temperature range is sufficiently high so that creep deformation is significant and may lead to the rupture of the specimen (at a lower temperature, the Ti64 alloy would exhibit logarithm creep that is exhausted before rupture). On the other hand, the martensite is supposed to be sufficiently stable in this temperature range (the usual heat treatments for stress relief and martensite decomposition are carried out at 700 °C). Thus, we are investigating the mechanical behaviour of the as-built martensite and its evolution. Furthermore, performing tests at these temperatures will allow us to make comparisons with existing studies in this

temperature range [25,30]. The tests were carried out up to rupture. Few experiments were interrupted in the secondary creep stage.

During the creep deformation, the load is kept constant and the stress state is fully non uniform in the specimen as indicate finite element analysis (FEA) which allow to map stress and strain states within the specimen all along the creep test [31]. However, it was shown that it is possible to extract a mean value of minimum creep strain rate/stress couple that compares well with such couples deduced from uniaxial tensile creep tests [13]. In the present study, we followed Kappou et al. [32] method for the determination of minimum deflection $\dot{u}_{min}$:

$$\dot{u}_{min} = \dot{u}_{1/2} = \frac{u_{2/3} - u_{1/3}}{1/2 t_f - 1/3 t_f} \quad (2)$$

where t_f is the time to failure, and $u_{2/3}$ and $u_{1/3}$ are, respectively, the deflection at $2/3t_f$ and $1/3t_f$.

From $\dot{u}_{min}$, we deduced the values of the minimum creep strain rate $\dot{\varepsilon}_{min}$ and stress σ using empirical equations and coefficients reported as Equations (3) and (4) [13].

$$\dot{\varepsilon}_{min} = 0.3922 \dot{u}^{1.191}_{min} \quad (3)$$

$$\sigma = \frac{F}{1.920 * u^{0.653}_{min}} \quad (4)$$

where u_{min} is the deflection at the minimum deflection rate.

3. Results & Discussion

Figure 2a shows the SPCT results obtained at 450 °C and an initial stress of 400 MPa, which corresponds to a load of 844 N.

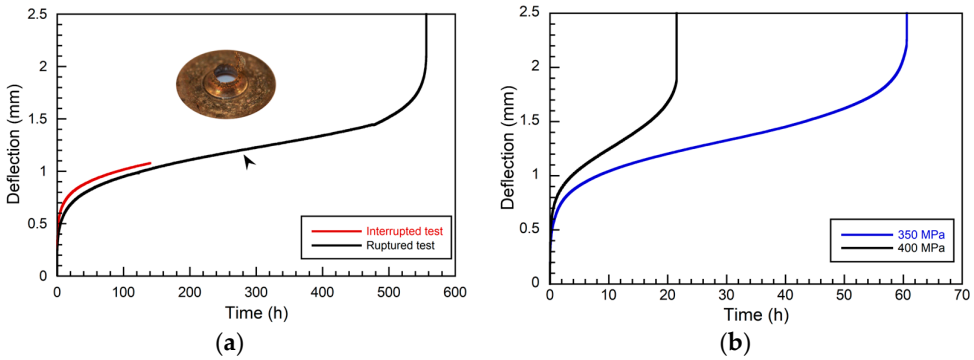

Figure 2. SPCT curves showing the evolution of deflection versus time for tests performed at 450 °C and $\sigma_{initial}$ = 400 MPa (**a**); SPCT curves showing the effect of the initial stress $\sigma_{initial}$ at 500 °C (**b**). Note the different time scale in both figures.

The black line is associated with a test conducted up to rupture. The whole curve looks very much like a uniaxial creep test curve showing the three conventional stages: primary, secondary, and tertiary creep regimes. The corresponding ruptured sample is shown as an insert in the figure. A second curve on the same graph is associated with an interrupted test that was performed under the same conditions (450 °C/400 MPa) but stopped after 140 h of creep. Is it worth noting that both curves exhibit the same trend concerning the primary stage and the beginning of the secondary stage, indicating the repeatability of the test. From the test conducted to rupture, we estimated the minimum deflection rate (at the point shown with an arrow on the graph in Figure 2a) which was measured as $1.17 \cdot 10^{-3}$ mm/h. From that value, we calculated the corresponding minimum creep rate $\dot{\varepsilon}_{min}$ = $3.52 \cdot 10^{-8}$ s^{-1} and stress σ = 388 MPa according to Equations (3) and (4). Figure 2b shows the SPCT results obtained at 500 °C and under initial stresses of 350 MPa

corresponding to a force of 728 N and under 400 MPa, corresponding to an initial force of 751 N. Similarly to what was observed at 450 °C, the curves exhibit the three conventional creep stages. Moreover, as the stress increases, the creep rate increases significantly and the time to failure decreases. As previously performed for the 450 °C tests, the minimum creep rates and corresponding stress were calculated. An initial stress of 350 MPa led to a minimum creep rate of $5.91 \cdot 10^{-7}$ s^{-1} for a stress value of 315 MPa, and an initial stress of 400 MPa led to $2.04 \cdot 10^{-6}$ s^{-1} and 388 MPa.

Those values are plotted on a Norton representation as shown in Figure 3, together with previous data from the literature [25], arising from uniaxial tensile creep tests performed on as-built L-PBF Ti64 specimens. The presented SPCT values are displayed using full symbols, while open symbols represent data from tensile tests. First of all, one can recognize that the data obtained in the present study are in line with previous data from tensile creep testing. Experiments from Viespoli et al. [25] were performed at the temperatures 650 °C, 550 °C, and 450 °C. From their results, the authors measured stress exponents of, respectively, n = 3.7, 4.8, and 5.8. The data from the present study align quite well with Viespoli et al.'s results for the 450 °C tests. The presented data from the tests performed at 500 °C lie between the uniaxial tests performed at 450 °C and 550 °C, which is fully consistent. A first estimate of the stress exponent derived from our two points obtained at 500 °C gives a value of 5.4 for a stress range of 300–400 MPa, in good agreement with the values obtained by Viespoli et al. Moreover, the higher the temperature, the lower the stress exponent, which also agrees with the literature on the creep of Ti64 [30]. These preliminary results, based on a few tests, indicate that SPCT seems to be well adapted to study the creep behaviour of L-PBF Ti64. From the range of stress exponent values, it appears that the creep mechanism in L-PBF Ti64 may be based on dislocation-driven plastic flow.

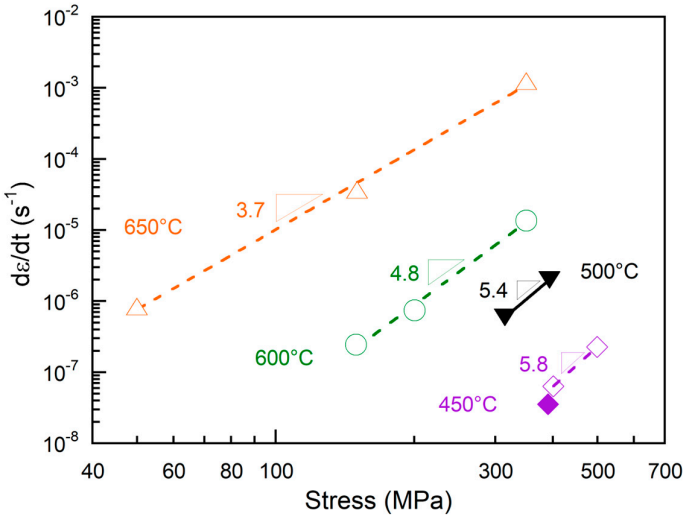

Figure 3. Comparison of present SPCT results (full symbols) with tensile creep tests results (open symbols) from Viespoli et al. [25] on as-built L-PBF Ti64.

Since the as-built microstructure of Ti64 presents an out-of-equilibrium martensitic microstructure, it is likely that such a microstructure may evolve during the creep test. Such evolution was characterised via SEM observation of interrupted SPCT specimen's cross-section. Interrupted tests and the characterisation of the microstructure were performed for SPCT conducted at both 450 and 500 °C. However, in the present paper, we focus on the microstructure evolution observed after 450 °C creeping. More precisely, we report observations performed on the interrupted SPCT presented with the red curve in Figure 2a. Indeed, in order to assess the effect of mechanical loading on the phase transformation, we selected a temperature for which we did not observe phase transformation without loading (unloaded heat treatment at 500 °C resulted in a slight transformation of the martensite with some small β particles forming at boundaries). The interrupted test specimen cross-section

was obtained by means of a cut through the centre of the deformed dome that was then embedded and prepared for metallographic observations. The central image in Figure 4 is a SEM secondary electron image showing half of the specimen cross-section gripped by clamping rings. The disc specimen is bent downwards by the deflection caused by the punch during SPCT. It is noticeable that the thickness of the section is not constant along the section, indicating inhomogeneous creep deformation. The upper left part, which was between the dies, did not undergo plastic deformation and retained its initial thickness (500 µm). The rest of the sample is more or less deformed. It can be seen that the thinnest section, i.e., the most deformed part—indicated by a white arrow—does not correspond to the apex at the bottom of the image but is located on the side of the dome, in good agreement with FEA calculations reported in the literature [31,33].

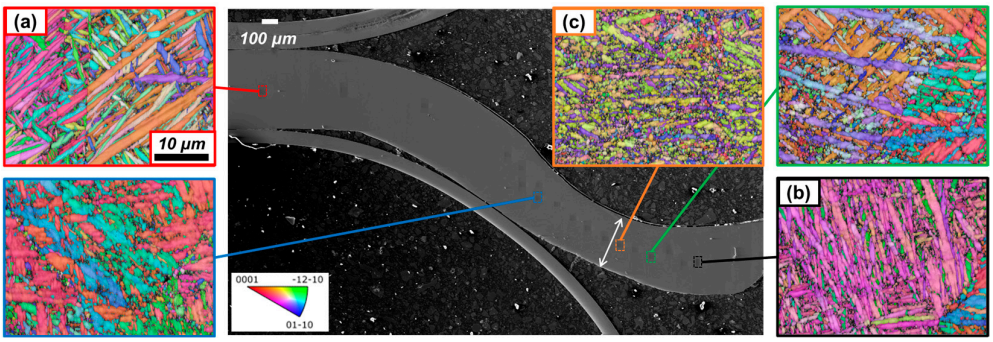

Figure 4. Cross-section of an SPCT specimen after interrupted test performed at 450 °C under $\sigma_{initial}$ = 400 MPa for 140 h. The IPF-Z images show the evolution of the microstructure depending on the location and associated strain level (see text). The location corresponding to the three images label (**a**–**c**) are examined in details in Figure 5.

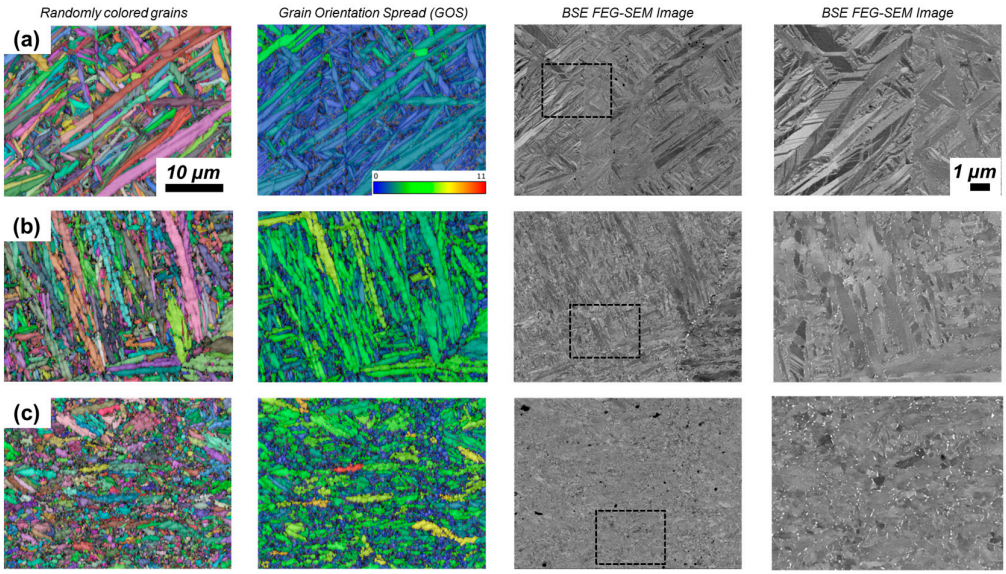

Figure 5. The three zones identified in Figure 3 are imaged using different signals: randomly coloured grains, grain orientation spread, and BSE FEG-SEM. The corresponding local creep strain levels are (**a**) 0.000, (**b**) 0.163, and (**c**) 0.358. See text for details.

The microstructure variations along the transverse section were observed via SEM EBSD and are presented in the five inserts showing the inverse pole figure along the z direction (normal to the image)—IPF-Z. Note that all EBSD images that are displayed in this paper include the mentioned signal (e.g., here IPF-Z), which is superimposed to the index quality map and large-angle grain boundaries. The IPF taken from the left part of the section shows the typical acicular feature of the martensitic microstructure (insert a).

Acicular microstructure is also retained at the top of the punched zone in insert b, while this microstructure is heavily disrupted in between with a paroxysm shown in insert c, which corresponds to the maximum of plastic strain. The microstructure of those three zones, a, b, and c, were analysed in more detail, as will be presented in Figure 5 below. From the cross-sectional thicknesses at the location of each zone, it is possible to associate each microstructure with a plastic deformation level. Zone a, located between the dies, is not deformed; zone b, located at the apex, corresponds to a creep strain of 16%, and zone c, to 36%. For this latter case, the literature on the FEA of SPCT indicates that the local strain level would even be higher than 36% since the strain is also heterogeneous over the disc thickness [31]. Figure 5 reports observations of these three zones using different observation conditions. In the two left-hand columns, we show EBSD analyses complementary to the IPF-Z. The images in the first column show the grains in random colours; adjacent grains are defined by a disorientation of 10°. This series clearly shows the overall changes in grain microstructure in terms of morphology and size along with the increase in creep strain. The second column is the grain orientation spread (GOS) angle, which reveals the amount of misorientation and thus the plastic strain within the grains. The two right-hand columns are SEM back-scattered electron (BSE) images, allowing higher resolution in order to visualize the fine microstructure. The third column corresponds to the same magnification and area as the EBSD maps, while the fourth column is a zoom on the selected area indicated by the dashed frame. These last images evidence the very fine morphology of the microstructure and reveal the decomposition of the α′ martensite that gives rise to the precipitation of β phase, visible with white contrast in those BSE images due to the higher V content. The evolution of the microstructure can be described as follows. In case (a), the microstructure remains martensitic and no change could be noticed as compared to the as-built state as reported in Figure 1. The martensitic microstructure is characterised by tangled lamellae with a high aspect ratio and quite a large distribution of lamellae sizes. The smallest ones are 80 nm wide by 1.3 μm long, while the largest are around 1 μm wide by up to 10 μm long and exhibit internal features that were identified as twins [27]. As the level of plastic/creep deformation increases, like in zone (b), the microstructure still shows an acicular aspect; however, significant changes occurred. The smaller needles have disappeared and are replaced by sub-micron globular grains, while the larger ones are fragmented. For the maximum of creep deformation, which corresponds to zone (c), the microstructure is completely transformed. Most of the grains are globular with a diameter around 250 nm. This transformation is associated with an evolution of the GOS values in the different grains of the microstructure. In Figure 5, the GOS values are indicated using the same colour scale for all three areas, allowing a direct comparison. The unstrained (a) area exhibits very small and quite uniform GOS values throughout the area analysed. In zone (b), the GOS values increase significantly in acicular regions but are very low in areas with globular grains. And finally, in zone (c), all the areas exhibiting nanograins show very low values of GOS. These observations clearly indicate that the nanograins were formed through dynamic recrystallisation during creep deformation. The column to the right in Figure 5 shows an increasing presence of the white precipitates which correspond to the β phase. Image analysis gives some rough estimate of the β phase volume content, which is less than 0.5% for zone a, around 1.5% for b, and 2.3% for zone c. There is a clear correlation between the volume fraction of the β phase and the amount of creep strain, evidencing the fact that plastic deformation locally enhances martensitic decomposition.

Microstructural observations subsequent to interrupted creep testing reveal two main features that were observed to be related to the amount of local creep deformation. These are (i) the decomposition of the α′ martensite to give the equilibrium phases α and β and (ii) the recrystallisation of the structure, modifying an entangled acicular structure to a globular nano-sized morphology. AM parts are often heat-treated to relieve internal stresses and stabilize the microstructure. This treatment is usually carried out for about one hour at a temperature of at least 700 °C. It induces a total decomposition of the α′ martensite and

a decrease in the yield strength [34]. Heat treatments performed at lower temperatures lead to partial and limited decomposition of the martensite [35]. However, it was noticed that martensite decomposition may be favoured during compression creep tests performed at 500 °C [24]. In the present study, we observed that complete decomposition of the martensite may be achieved in those areas that undergo maximum plastic strain. The present observations prove that local plastic strain enhances phase transformation and allows a complete transformation of the α′ martensite, even at temperatures as low as 450 °C.

The optimisation of the thermomechanical processes of α/β titanium alloys is of continuous concern in order to optimize their mechanical properties [36]. In particular, obtaining an ultrafine microstructure in such alloys enables superplastic behaviour. In Ti64 cast and wrought alloys, the possibility to obtain a sub-micrometre equiaxed microstructure was demonstrated [37,38]. The best results have been obtained through the transformation of martensitic microstructures [39,40]. These observations were related to the phenomenon of dynamic recrystallisation on martensitic microstructures occurring during compression tests performed in the temperature range 600–800 °C. In the present study, we observed dynamic recrystallisation of the α′ martensite at much lower temperature (450 °C). This results in a fully equiaxed microstructure with grain size well below the micron scale (250 nm) and an even distribution of β phase as shown in Figure 5c. The present results show that for such a low temperature, the progress of martensite decomposition and microstructure refinement strongly depends on the mechanical state, in particular, the local plastic strain. Work is in progress with the help of finite element calculations in order to quantify the correlation between mechanical state and local phase transformation. Further investigations are also underway using transmission electron microscopy. This is necessary to characterise the microstructure evolution within the transformed areas in a finer way and to assess the role of defects such as dislocations on phase transformation and martensite decomposition.

4. Conclusions

In this paper, we report the first creep characterisation of additive manufactured Ti64 using the SPCT technique. Preliminary creep results obtained through SPCT are in line with tensile creep test results, comforting the relevance of small punch testing in the case of AM Ti alloys. Microstructural evolution analysis was performed on an interrupted creep test specimen and showed that plasticity induced phase transformation. The plastic strain gradient within the SPCT sample shows that the decomposition of the α′ martensite is assisted by the creep strain level. Thanks to the plastic deformation, the decomposition of the martensite is complete even at temperatures as low as 450 °C. Furthermore, this process induces an equiaxed nanosized α + β microstructure due to dynamic recrystallisation.

Author Contributions: Methodology and investigation, M.L. and B.V.; validation, M.L., B.M. and B.V.; formal analysis, M.L., B.M. and B.V.; writing—original draft preparation, M.L.; writing—review and editing, M.L., B.M. and B.V.; supervision, B.V. All authors have read and agreed to the published version of the manuscript.

Funding: This research received no external funding.

Data Availability Statement: The data that support the findings of this study are available on request from the corresponding author: please contact mathieu.lale@toulouse-inp.fr.

Conflicts of Interest: The authors declare no conflict of interest.

References

1. Banerjee, D.; Williams, J.C. Perspectives on Titanium Science and Technology. *Acta Mater.* **2013**, *61*, 844–879. [CrossRef]
2. Boyer, R.R. An overview on the use of titanium in the aerospace industry. *Mater. Sci. Eng. A* **1996**, *213*, 103–114. [CrossRef]
3. Dareh Baghi, A.; Nafisi, S.; Ebendorff-Heidepriem, H.; Ghomashchi, R. Microstructural Development of Ti-6Al-4V Alloy via Powder Metallurgy and Laser Powder Bed Fusion. *Metals* **2022**, *12*, 1462. [CrossRef]

4. Barriobero-Vila, P.; Artzt, K.; Stark, A.; Schell, N.; Siggel, M.; Gussone, J.; Kleinert, J.; Kitsche, W.; Requena, G.; Haubrich, J. Mapping the geometry of Ti-6Al-4V: From martensite decomposition to localized spheroidization during selective laser melting. *Scr. Mater.* **2020**, *182*, 48–52. [CrossRef]
5. Munk, J.; Breitbarth, E.; Siemer, T.; Pirch, N.; Häfner, C. Geometry Effect on Microstructure and Mechanical Properties in Laser Powder Bed Fusion of Ti-6Al-4V. *Metals* **2022**, *12*, 482. [CrossRef]
6. Lucas, G.E. Review of small specimen test techniques for irradiation testing. *Met. Mater Trans A* **1990**, *21*, 1105–1119. [CrossRef]
7. Manahan, M.P.; Argon, A.S.; Harling, O.K. The development of a miniaturized disk bend test for the determination of postirradiation mechanical properties. *J. Nucl. Mater.* **1981**, *104*, 1545–1550. [CrossRef]
8. Dymáček, P. Recent developments in small punch testing: Applications at elevated temperatures. *Theor. Appl. Fract. Mech.* **2016**, *86*, 25–33. [CrossRef]
9. Dobeš, F.; Dymáček, P.; Besterci, M. Estimation of the mechanical properties of aluminium and an aluminium composite after equal channel angular pressing by means of the small punch test. *Mater. Sci. Eng. A* **2015**, *626*, 313–321. [CrossRef]
10. Bártková, D.; Langer, J.; Dymáček, P.; Válka, L. Determination of Mechanical Properties of Magnesium Alloys and Composites by Small Punch Testing. *Appl. Mech. Mater.* **2016**, *821*, 435–441. [CrossRef]
11. Shen, Y.; Lv, S.; Zhou, Q.; Shi, L.; Sun, L.; Li, Z. Microstructure Characterization and Small Punch Test Analysis in Nickel-Based Alloy 617 by High Energy Neon Implantation. *Metals* **2022**, *12*, 438. [CrossRef]
12. Dymáček, P.; Dobeš, F.; Jarý, M.; Jirásková, Y.; Pizúrová, N.; Friák, M. Small punch testing of Fe-Al based alloys with Ti and Nb additions. *IOP Conf. Ser. Mater. Sci. Eng.* **2020**, *723*, 012006. [CrossRef]
13. Bruchhausen, M.; Austin, T.; Holmstrom, S.; Altstadt, E.; Dymacek, P.; Jeffs, S.; Lancaster, R.; Lacalle, R.; Matocha, K.; Petzova, J. European standard on small punch testing of metallic materials. In Proceedings of the ASME 2017—Pressure Vessels and Piping Conference, Waikoloa, HI, USA, 16–20 July 2017; p. 1A-2017. [CrossRef]
14. *NF EN 10371*; Matériaux Métalliques—Méthode d'essai de Micro-Emboutissage. Association Française de Normalisation (AFNOR): La Plaine Saint-Denis, France, 2021.
15. Tian, X.; Zhang, S.; Xu, H.; Li, T.; Yang, B.; Zhang, M. Assessment of Creep Properties Using Small Punch Test for a 9%Cr-Mo-Co-B Power Plant Steel. *Metals* **2021**, *11*, 1996. [CrossRef]
16. Dobeš, F.; Dymáček, P. Fracture-based correlation of uniaxial and small punch creep data. *Theor. Appl. Fract. Mech.* **2016**, *86*, 34–38. [CrossRef]
17. Dymáček, P. Short Term Creep Small Punch Testing of P91 and P92 Steels, Observations and Correlations with the Numerical Results. *Key Eng. Mater.* **2011**, *465*, 179–182. [CrossRef]
18. Dobeš, F.; Milička, K. Application of creep small punch testing in assessment of creep lifetime. *Mater. Sci. Eng. A* **2009**, *510–511*, 440–443. [CrossRef]
19. Holmström, S.; Li, Y.; Dymacek, P.; Vacchieri, E.; Jeffs, S.P.; Lancaster, R.J.; Omacht, D.; Kubon, Z.; Anelli, E.; Rantala, J.; et al. Creep strength and minimum strain rate estimation from Small Punch Creep tests. *Mater. Sci. Eng. A* **2018**, *731*, 161–172. [CrossRef]
20. Peng, J.; Gao, M.; Zhang, H.; Geng, X.; Liu, X.; Pan, H. Small punch creep test reveals the differences of high-temperature creep behaviours for laser powder bed fusion and Rolled Inconel 718 alloys. *Mater. Sci. Eng. A* **2023**, *886*, 145698. [CrossRef]
21. Lancaster, R.J.; Illsley, H.W.; Davies, G.R.; Jeffs, S.P.; Baxter, G.J. Modelling the small punch tensile behaviour of an aerospace alloy. *Mater. Sci. Technol.* **2016**, *33*, 1065–1073. [CrossRef]
22. Lucon, E.; Benzing, J.; Hrabe, N. *Small Punch Testing to Estimate Mechanical Properties of Additively Manufactured Ti-6Al-4V*; US Department of Commerce, National Institute of Standards and Technology: Washington, DC, USA, 2020. [CrossRef]
23. Illsley, H.; Lancaster, R.; Jeffs, S.; Baxter, G. Small Punch Testing of Electron Beam Melted (EBM) Ti-6Al-4V. In Proceedings of the 13th World Conference on Titanium, San Diego, CA, USA, 16–20 August 2016; pp. 1401–1406. [CrossRef]
24. Kim, Y.K.; Park, S.H.; Yu, J.H.; AlMangour, B.; Lee, K.A. Improvement in the high-temperature creep properties via heat treatment of Ti-6Al-4V alloy manufactured by selective laser melting. *Mater. Sci. Eng. A* **2018**, *715*, 33–40. [CrossRef]
25. Viespoli, L.M.; Bressan, S.; Itoh, T.; Hiyoshi, N.; Prashanth, K.G.; Berto, F. Creep and high temperature fatigue performance of as build selective laser melted Ti-based 6Al-4V titanium alloy. *Eng. Fail. Anal.* **2020**, *111*, 104477. [CrossRef]
26. Spigarelli, S.; Paoletti, C.; Cabibbo, M.; Cerri, E.; Santecchia, E. On the creep performance of the Ti-6Al-4V alloy processed by additive manufacturing. *Addit. Manuf.* **2022**, *49*, 102520. [CrossRef]
27. Wang, H.; Chao, Q.; Yang, L.; Cabral, M.; Song, Z.Z.; Wang, B.Y.; Primig, S.; Xu, W.; Chen, Z.B.; Ringer, S.P.; et al. Introducing transformation twins in titanium alloys: An evolution of α-variants during additive manufacturing. *Mater. Res. Lett.* **2021**, *9*, 119–126. [CrossRef]
28. Mahmud, A.; Huynh, T.; Zhou, L.; Hyer, H.; Mehta, A.; Imholte, D.D.; Woolstenhulme, N.E.; Wachs, D.M.; Sohn, Y. Mechanical Behavior Assessment of Ti-6Al-4V ELI Alloy Produced by Laser Powder Bed Fusion. *Metals* **2021**, *11*, 1671. [CrossRef]
29. Lalé, M.; Viguier, B. Mechanical properties assessment of additively manufactured Ti64 alloy using Small Punch Tests. *Mater. High Temp.* **2023**. submitted.
30. Badea, L.; Surand, M.; Ruau, J.; Viguier, B. Creep Behavior of Ti-6Al-4V FROM 450 °C TO 600 °C. *UPB Sci. Bull. Ser. B* **2014**, *76*, 185–196.
31. Dymáček, P.; Milička, K. Creep small-punch testing and its numerical simulations. *Mater. Sci. Eng. A* **2009**, *510–511*, 444–449. [CrossRef]

32. Kappou, E.; Holmstrom, S. *Small Punch Creep Tests for Grade 92 Forgings*; EUR 29360 EN; Publications Office of the European Union: Luxembourg, 2018. [CrossRef]
33. Lancaster, R.J.; Jeffs, S.P.; Haigh, B.J.; Barnard, N.C. Derivation of material properties using small punch and shear punch test methods. *Mater. Des.* **2022**, *215*, 110473. [CrossRef]
34. Dumontet, N.; Connétable, D.; Malard, B.; Viguier, B. Elastic properties of the α' martensitic phase in the Ti-6Al-4V alloy obtained by additive manufacturing. *Scr. Mater.* **2019**, *167*, 115–119. [CrossRef]
35. Wu, S.Q.; Lu, Y.J.; Gan, Y.L.; Huang, T.T.; Zhao, C.Q.; Lin, J.J.; Guo, S.; Lin, J.X. Microstructural evolution and microhardness of a selective-laser-melted Ti–6Al–4V alloy after post heat treatments. *J. Alloys Compd.* **2016**, *672*, 643–652. [CrossRef]
36. Semiatin, S.L. An Overview of the Thermomechanical Processing of α/β Titanium Alloys: Current Status and Future Research Opportunities. *Met. Mater Trans A* **2020**, *51*, 2593–2625. [CrossRef]
37. Zherebtsov, S.; Murzinova, M.; Salishchev, G.; Semiatin, S.L. Spheroidization of the lamellar microstructure in Ti–6Al–4V alloy during warm deformation and annealing. *Acta Mater.* **2011**, *59*, 4138–4150. [CrossRef]
38. Park, C.H.; Kim, J.H.; Yeom, J.-T.; Oh, C.-S.; Semiatin, S.L.; Lee, C.S. Formation of a submicrocrystalline structure in a two-phase titanium alloy without severe plastic deformation. *Scr. Mater.* **2013**, *68*, 996–999. [CrossRef]
39. Gu, J.L.; Sun, X.J.; Bai, B.Z.; Chen, N.P. Microstructural evolution during fabrication of ultrafine grained alpha+beta titanium alloy. *Mater. Sci. Technol.* **2001**, *17*, 1516–1524. [CrossRef]
40. Chao, Q.; Hodgson, P.D.; Beladi, H. Ultrafine Grain Formation in a Ti-6Al-4V Alloy by Thermomechanical Processing of a Martensitic Microstructure. *Met. Mater. Trans. A* **2014**, *45*, 2659–2671. [CrossRef]